Representation of Topography in Spectral Climate Models and Its Effect on Simulated Precipitation

CRAIG LINDBERG

Program in Atmospheric and Oceanic Sciences, Princeton University, Princeton, New Jersey

ANTHONY J. BROCCOLI

Geophysical Fluid Dynamics Laboratory/NOAA, Princeton University, Princeton, New Jersey

(Manuscript received 31 January 1995, in final form 19 April 1996)

ABSTRACT

Spectral climate models are distinguished by their representation of variables as finite sums of spherical harmonics, with coefficients computed by an orthogonal projection of the variables onto the spherical harmonics. Representing the surface elevation in this manner results in its contamination by Gibbs-like truncation artifacts, which appear as spurious valleys and mountain chains in the topography. These "Gibbs ripples" are present in the surface topographies of spectral climate models from a number of research institutions. Integrations of the Geophysical Fluid Dynamics Laboratory (GFDL) climate model over a range of horizontal resolutions indicate that the Gibbs ripples lead to spurious, small-scale extrema in the spatial distribution of precipitation. This "cellular precipitation pathology" becomes more pronounced with increasing horizontal resolution, causing a deterioration in the fidelity of simulated precipitation in higher resolution models.

A method is described for reducing the Gibbs ripples that occur when making an incomplete spherical harmonic expansion of the topography. The new spherical harmonic representations of topography are formed by fitting a nonuniform spherical smoothing spline to geodetic data and found by solving a fixed-point problem. This regularization technique results in less distortion of features such as mountain height and continental boundaries than previous smoothing methods. These new expansions of the topography, when used as a lower boundary surface in the GFDL climate model, substantially diminish the cellular precipitation pathology and produce markedly more realistic simulations of precipitation. These developments make the prospect of using higher resolution spectral models for studies of regional hydrologic climate more attractive.

1. Introduction

The spectral transform method has been widely used in atmospheric general circulation models, both for weather forecasting and climate simulation. In this method, the horizontal values of meteorological variables are approximated as a truncated series of analytic functions, such as the surface spherical harmonics, more commonly called the spherical harmonics. Spectral methods are more accurate and stable than finite element and finite difference methods, and have several other advantages as well (Canuto et al. 1988). Thus, it is likely that the spectral transform method (also known as the semispectral method) will continue to be a common numerical procedure used in atmospheric circulation models.

A difficulty arises, however, in the representation of surface boundary conditions in atmospheric spectral models. In the spectral method, the earth's surface is represented as an incomplete expansion in spherical harmonics with the coefficients determined by an orthogonal projection of the surface onto the spherical harmonics. The earth's surface is arbitrarily irregular and, therefore, can be only approximated by a truncated series of orthogonal functions. This incompleteness of the basis set manifests itself in the model as an unfaithful portrayal of the peaks and valleys in the topography at a given resolution, as well as the contamination of the model with spurious oscillations in the neighborhood of topographic features of substantial relief, as identified by Hoskins (1980).

These spurious oscillations are similar to the Gibbs effect in truncated Fourier series, and therefore we refer

* Current affiliation: IDA/Center for Computing Sciences, University of Maryland Science and Technology Center, Bowie, Maryland.

Corresponding author address: Anthony J. Broccoli, GFDL/NOAA, Princeton University, P.O. Box 308, Princeton, NJ 08542. E-mail: ajb@gfdl.gov

to them as Gibbs ripples or Gibbs oscillations. They appear as rolls with their long axes oriented north–south for topographic features that are predominantly aligned north–south (such as the Andes; these Gibbs oscillations are called zonal Gibbs ripples) and as rolls extending east–west for topographic features that are aligned east–west (such as the steep slope at the periphery of the Antarctic ice sheet; these are referred to as meridional Gibbs ripples). Obviously, since the earth's topography includes more irregular features than simple latitudinally or longitudinally oriented mountain ranges, the spurious Gibbs oscillations can take on a fairly complicated character, as oscillations beat against each other and interfere constructively and destructively.

Navarra et al. (1994) have shown that effects of these Gibbs oscillations are evident in long integrations of dynamical forecasting models and may contribute to discrepancies between the simulated and observed climates. They have shown that precipitation, wind, and water vapor mixing ratio are among the quantities that are affected by the Gibbs oscillations. In order to reduce these oscillations, Navarra et al. (1994) describe a number of spectral coefficient weighting schemes for use in constructing the spectral model topography. They present results from an extended model integration using one of these methods (the so-called isotropic filter) that shows a distinct reduction of the Gibbs oscillation signature in the atmospheric variables.

This paper extends the work of Navarra et al. (1994) by examining in more detail the sensitivity of simulated precipitation to the representation of topography in a spectral climate model. We demonstrate that serious deficiencies can arise when spectral model topography is a truncated series of spherical harmonics with coefficients produced by an orthogonal projection of the gridpoint surface elevation values onto the spherical harmonics. A new method of representing topography is developed that greatly reduces the Gibbs oscillations while preserving the elevation of major topographic features with more fidelity than previous attempts. Results from an extended climate simulation using this representation are presented to evaluate its effectiveness in producing a realistic distribution of simulated precipitation. We also offer some suggestions for further improvement in the design of spectral model topography.

This report is organized as follows. A brief introduction to the representation of the horizontal values of atmospheric variables by spherical harmonics is given in section 2. Section 3 describes the climate model used in our numerical experiments, and section 4 discusses the origin and preparation of the basic gridded topographic dataset. Section 5 illustrates how simulated precipitation is adversely affected when topography is produced by an orthogonal projection onto a restricted set of spherical harmonics. In section 6, we propose a new technique for representing topography and compare it to the existing alternatives. The results of climate model integrations utilizing various topographic representations are presented in section 7, followed by some suggestions for future work in section 8. A concluding discussion in contained in section 9.

2. Spectral representation of atmospheric variables

Both physical space and spectral space versions of a number of basic variables are computed in spectral global climate models. In physical space, a variable x is represented as a set of values on a latitude–longitude grid (often called the transform grid).[1]

An arbitrary square-integrable function on the sphere $x(\phi, \lambda)$ can be expanded as a series of surface spherical harmonics:

$$x(\phi, \lambda) = \sum_{l=0}^{\infty} \sum_{m=-l}^{l} b_{lm} Y_{lm}(\phi, \lambda) \qquad (2.1)$$

where $Y_{lm}(\phi, \lambda)$ is an orthogonal spherical harmonic of degree (meridional wavenumber) l and azimuthal order (zonal wavenumber) m (Hobson 1931; Jones 1985). The spherical harmonics are orthonormal with respect to the solid angle measure $d\Omega = \sin\phi d\phi d\lambda$ on the sphere S_2, so the coefficients b_{lm} can be expressed as the orthogonal projection with respect to $d\Omega$ of the variable $x(\phi, \lambda)$ onto the spherical harmonics:

$$b_{lm} = \int_{S_2} x(\phi, \lambda) Y^*_{lm}(\phi, \lambda) d\Omega, \qquad (2.2)$$

where the asterisk superscript denotes complex conjugation. The set of coefficients $\{b_{lm}\}$ form the spectral space version of the physical space quantity $x(\phi, \lambda)$. In atmospheric spectral models, the series (2.1) must be truncated, traditionally to form either a triangular truncation model

$$x_T(\phi, \lambda) = \sum_{l=0}^{M} \sum_{m=-l}^{l} b_{lm} Y_{lm}(\phi, \lambda) \qquad (2.3)$$

or a rhomboidal truncation model

$$x_R(\phi, \lambda) = \sum_{m=-M}^{M} \sum_{l=|m|}^{|m|+M} b_{lm} Y_{lm}(\phi, \lambda). \qquad (2.4)$$

The truncated expansions (2.3) and (2.4) approximate the series (2.1). Figure 1 depicts the terms that contribute to the triangular and rhomboidal sums on the l–m plane for $M = 21$ and $M = 15$, respectively, dem-

[1] These values are denoted in conventional notation as $\{x(\phi_j, \lambda_k)\}_{j=1,k=1}^{J,K}$ where ϕ_j is colatitude (i.e., $\phi_j = 0$ at the North Pole and $\phi_j = \pi$ at the South Pole) with values ordered so that $0 \leq \phi_j < \phi_{j+1} \leq \pi$, $j = 1, 2, \cdots, J-1$ and λ_k is longitude, with $0 \leq \lambda_k < \lambda_{k+1} \leq 2\pi$, $k = 1, 2, \cdots, K-1$. The transform grid consists of the J, K ordered pairs $\{(\phi_j, \lambda_k)\}_{j=1,k=1}^{J,K}$. The spacing of the transform grid is $\Delta_\phi(j)$ by $\Delta_\lambda(k)$, where $\Delta_\phi(j) = \phi_{j+1} - \phi_j$ and $\Delta_\lambda(k) = \lambda_{k+1} - \lambda_k$.

onstrating graphically why these two truncated expansions have been given these names. On a transform grid, relations analogous to (2.1)–(2.4) hold. (In the following sections, continuous formulae will be used to represent their discrete analogues to reduce notational complexity.)

3. Climate model description

A version of the climate model of the Geophysical Fluid Dynamics Laboratory very similar to that of Broccoli and Manabe (1992) was used in this study. This model consists of two basic units: 1) a general circulation model of the atmosphere and 2) a heat and water balance model over the continents. The oceanic component of the climate system was not modeled explicitly; instead, the geographical distribution of sea surface temperature and sea ice was prescribed, varying seasonally, in a manner consistent with observations.

As previously mentioned, the atmospheric model employs the spectral transform method, and therefore the horizontal values of the basic atmospheric variables are represented as a truncated or incomplete series of spherical harmonics. In most of the experiments described here, the rhomboidal expansion retaining $M = 30$ zonal waves is employed to represent the basic variables. (For brevity, rhomboidal truncation at zonal wavenumber $M = 30$ is subsequently designated as R30 truncation; an analogous nomenclature is used for triangular truncation.) The spacing of the R30 transform grid is approximately 2.25° latitude by 3.75° longitude. Normalized pressure (σ) is used as the model's vertical coordinate, with variables computed at nine unevenly spaced levels and vertical derivatives formed by finite differences of the values at these levels. The dynamical component of this model was developed by Gordon and Stern (1982) and is very similar to that described by Bourke (1974).

Solar radiation at the top of the atmosphere is prescribed, varying seasonally but not diurnally. Computation of the flux of solar radiation is performed using a method similar to that of Lacis and Hansen (1974) except that the bulk optical properties of various cloud types are specified. Terrestrial radiation is computed as described by Stone and Manabe (1968). For the computation of radiative transfer clouds are prescribed, varying only with height and latitude. The mixing ratio of carbon dioxide is assumed constant everywhere, and the ozone mixing ratio is specified as a function of height, latitude, and season.

Over the continents, surface temperatures are computed from a heat balance with the requirement that no heat is stored in the soil. Both snow cover and soil moisture are predicted. A change in snow depth is computed as the net contribution from snowfall, sublimation, and snowmelt, with the latter two determined from the surface heat budget. Soil moisture is calculated by the "bucket method." The soil is assumed to have a water holding capacity of 15 cm. If the computed soil moisture exceeds this amount, the excess is assumed to be runoff. Changes in soil moisture are obtained from the rates of rainfall, evaporation, snowmelt, and runoff. Evaporation from the soil is determined as a function of soil moisture and the potential evaporation rate (i.e., the hypothetical evaporation rate from a completely wet soil). Further details of the hydrologic computations can be found in Manabe (1969).

4. Topographic data

The topographic data used throughout the current experiments were derived from a high resolution ($1/6°$ by $1/6°$) geodetic dataset prepared by the U.S. Navy (Cuming and Hawkins 1981). For generating the R30 topographic representations discussed in this paper, the first step was the preparation of surface elevation data on an R30 transform grid. This was accomplished by assuming that each transform grid point defines the center of a grid box, determining which high resolution grid points lay within that box, forming an arithmetic mean of these high resolution terrain heights, and assigning the resulting average elevation to the transform grid point. The dataset resulting from this aggregation of the $1/6°$ resolution Navy data is the ultimate source of most of the various representations of topography discussed in subsequent sections.

For other resolutions, we present results from preexisting climate model integrations, which utilized a slightly different procedure for calculating the surface height values on the transform grid. To prepare the spectral topography for these integrations the $1/6°$ resolution Navy topographic data were aggregated to a grid of substantially higher resolution than the model, using the procedure described above. A comparison indicates that the resulting spectral topography does not appear sensitive to the difference between these two procedures.

5. Standard topography and its effect on precipitation

The standard method for forming truncated spherical harmonic representation of the topography is to use (2.3) or (2.4) with the coefficients $\{b_{lm}\}$ computed by the orthogonal projection on the spherical harmonics (2.2). As Navarra et al. (1994) have shown, topography designed in this fashion is contaminated by Gibbs oscillations. These oscillations arise because there are more degrees of freedom in the values on a transform grid than in the truncated set of spherical harmonics.

Figure 2 depicts the standard topography at R30 resolution as computed by the procedure described in section 4, followed by the use of (2.2) and (2.4). The Gibbs oscillations are plainly visible, most prominently as north–south bands parallel to the Andes over the eastern South Pacific and east–west bands just north of

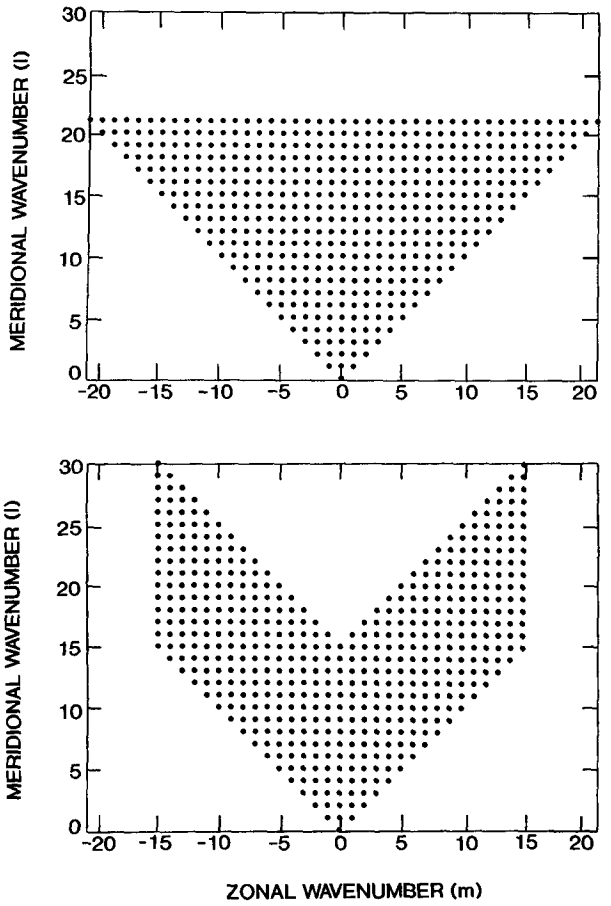

FIG. 1. The values of the meridional wavenumber l and the zonal wavenumber m for each term included in a truncated sum of spherical harmonics corresponding to a point on the l–m plane, marked with a dot. Top: terms in a T21 sum (triangular truncation at $M = 21$). Bottom: terms in an R15 sum (rhomboidal truncation at $M = 15$).

the Antarctic continent. The crests (troughs) of these oceanic Gibbs ripples can be as much as 200 m above (below) sea level. Smaller-scale features are also apparent throughout the oceans. As demonstrated in detail in section 7, similar oscillations occur over the continents, although they are not as readily apparent due to the complexity of continental terrain.

The generation of spectral model topography by this procedure has been widely used, as demonstrated by a survey of model results produced for the Atmospheric Model Intercomparison Project (Gates 1992). Figure 3 depicts cross sections of surface elevation across the Andes and adjacent regions from T42 (triangular spectral truncation at wavenumber $M = 42$) integrations supplied by the National Meteorological Center[2] (U.S.), European Centre for Medium-Range Weather Forecasts (U.K.), Max Planck Institute for Meteorology (Germany), Centre National de Recherches Météorologiques (France) and the National Center for Atmospheric Research (U.S.). Standard topography computed by the procedure described in section 4 is also included for comparison. These cross sections demonstrate that similar Gibbs oscillations are found in topographies used throughout the spectral climate modeling community, despite the occasional use of simple filters to reduce the amplitude of high wavenumber components, as in the National Center for Atmospheric Research model (Boville 1991). Comparable oscillations are present in topographies (not shown) taken from integrations supplied by the Bureau of Meteorology Research Centre (Australia), Canadian Climate Centre, Commonwealth Scientific and Industrial Research Organisation (Australia), and the State University of New York at Albany (U.S.).

The standard topography formed by orthogonal projection was used to conduct three climate model integrations with horizontal resolutions of R15, R30, and R63. The lengths of these integrations are 10, 5, and 5 years, respectively. Other aspects of the integrations are identical. The simulated annual mean precipitation from each of these integrations is depicted in Fig. 4, along with the observed precipitation climatology of Legates and Willmott (1990).

Dramatic differences are evident when comparing the three simulations and the observed climatology. As the horizontal resolution increases, the tendency for precipitation to be organized in a cellular structure becomes more pronounced, particularly over land. Over the oceans, a structure of closely spaced bands also becomes evident as resolution is increased. These unusual patterns are similar in appearance to the structure of the Gibbs oscillations in the standard topography (Fig. 2) and are not present in the observed climatology.

As a result of this "cellular precipitation pathology," the similarity between the simulated and observed precipitation decreases with increasing horizontal resolution. A quantitative measure of this decrease can be obtained by interpolating or aggregating the simulated and observed precipitation to a common grid and computing an area-weighted pattern correlation. Hulme (1991) used a very similar technique in comparing precipitation simulated by various climate models with observed data. In the current analysis, a $1° \times 1°$ grid was used as a common grid. The Legates and Willmott data are of higher resolution, so they were aggregated to the $1° \times 1°$ grid. All three model grids are of lower resolution, so the simulated precipitation from each was interpolated to the common grid. Based on this procedure, the pattern correlations between the simulated and observed annual mean precipitation are 0.717, 0.660, and 0.549 for R15, R30, and R63, respectively. Root-mean-square differences between the simulated and observed annual mean precipitation are

[2] Now known as the National Centers for Environmental Prediction.

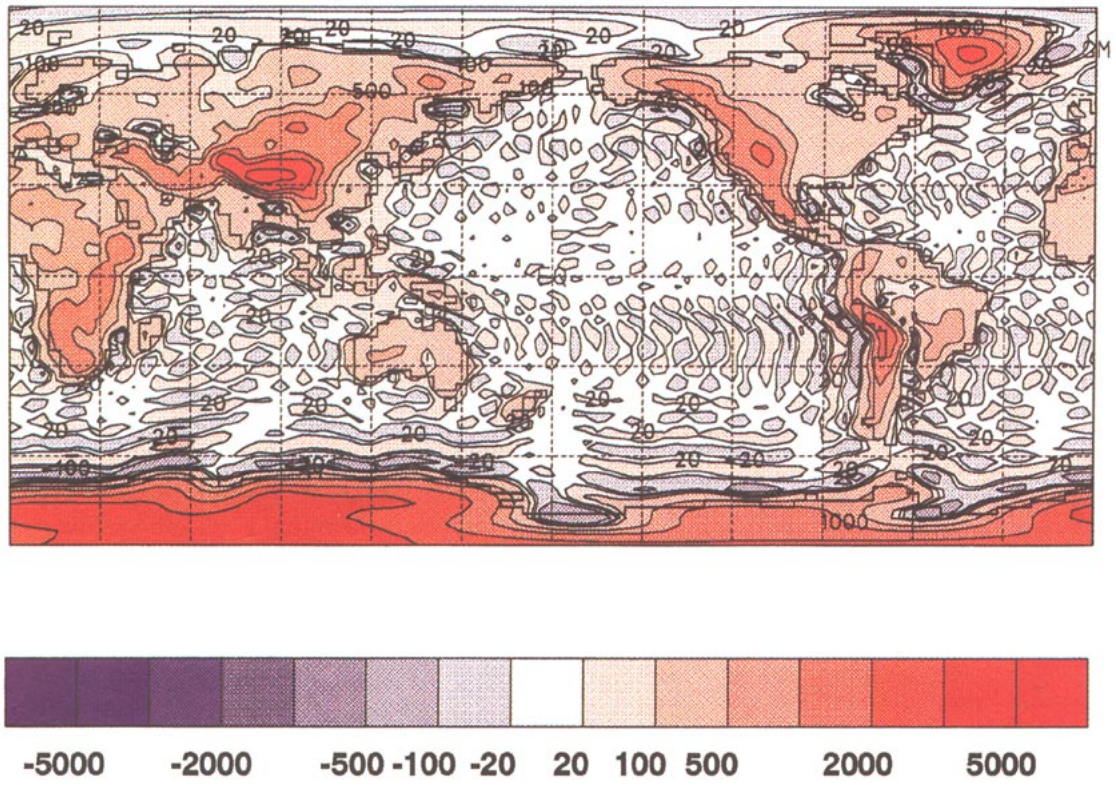

FIG. 2. R30 climate model surface elevation (m) computed using the standard procedure.

0.180, 0.209, and 0.263 cm/day for R15, R30, and R63, respectively. As the resolution of the model increases, the pattern correlation decreases and rms difference increases, indicating that greater resolution leads to less realistic simulations of precipitation.

Evidence of the cellular precipitation pathology is present in spectral space as well as in physical space. To illustrate this perspective, contour plots of the fraction of total variance of annual mean precipitation $P(\phi, \lambda)$ associated with each spherical harmonic are exhibited:

$$B_{lm} = \frac{|\rho_{lm}|^2}{\sum'_{l',m'} |\rho_{l'm'}|^2}, \qquad (5.1)$$

where $\rho_{lm} = \int_{S_2} Y_{lm}(\phi, \lambda) P(\phi, \lambda) d\Omega$. ($\Sigma'$ denotes a truncated sum. We focus on the use of rhomboidally truncated series in this paper, although the methods we describe are equally appropriate for triangular truncation.) We have dubbed this quantity B_{lm} a "spherical periodogram" of $P(\phi, \lambda)$ because of its similarity to the traditional periodogram. Figure 5 displays spherical periodograms of precipitation for the R30 model with the standard topography and also for the Legates and Willmott (1990) observed climatology. Zonal wavenumber m lies along the abscissa and the shifted meridional wavenumber $l - |m|$ on the ordinate.

Comparison of spherical periodograms of simulated and observed precipitation reveals both similarities and substantial differences. In both cases the largest fractional variance appears toward the lower left corner of the plot, representing low zonal and meridional wavenumbers. The fractional variance in the observed precipitation decreases rapidly with increasing wavenumber, particularly along the zonal axis. (The less rapid decrease in fractional variance along the ordinate at low zonal wavenumbers is indicative of a tendency for precipitation to be organized in east–west bands when averaged over long time periods.) The major difference between these two spherical periodograms is that the fractional variance of simulated precipitation does not decrease as rapidly with increasing wavenumber, as indicated by the preponderance of blue rather than gray in the upper right quadrant of the plot. This is a signature of the greater precipitation variance associated with small spatial scales in the model simulation.

The systematic decrease in the fidelity of precipitation simulation with increasing resolution is inconsistent with the expectation that higher resolution models would better simulate small-scale features of the earth's climate. It also suggests that this cellular precipitation pathology constitutes a major obstacle to the simulation of hydrologic quantities on regional and smaller scales.

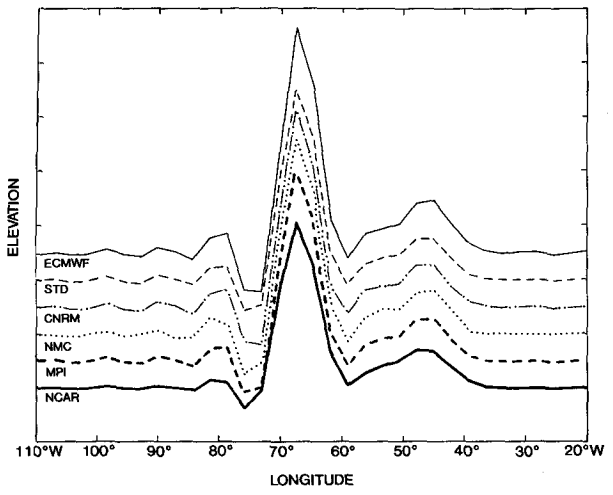

FIG. 3. Surface elevation profiles (m) along 21°S between 105° and 25°W from five different T42 climate models, with standard topography (computed by orthogonal projection) included for comparison. Tick marks on the vertical axis are every 1000 m, and an offset of 500 m is used between each elevation profile. (CNRM: Centre National de Recherches Météorologiques; ECMWF: European Centre for Medium-Range Weather Forecasts; MPI: Max Planck Institute for Meteorology; NCAR: National Center for Atmospheric Research; NMC: National Meteorological Center; STD: standard topography.)

Based on the hypothesis that this pathology is associated with the existence of large Gibbs oscillations in the standard topography, in the next section we explore other methods for representing model topography that reduce these oscillations and their impact on simulated precipitation.

6. Reducing Gibbs oscillations in spectral model topography

A possible method for reducing the Gibbs truncation artifacts in the topography is to choose the spectral coefficients in some way that reduces the truncation effects. One approach is to incorporate the desired physical properties into a penalty function whose minimum defines the spectral coefficients. Effectively, the desired physical properties are used to choose a more useful metric than the standard squared distance between the gridpoint surface and a spectral representation of that surface.

Given a topography $x(\phi, \lambda)$ (suppressing the subscripts on the arguments), one wishes to choose coefficients a_{lm} so that $x(\phi, \lambda)$ is approximated by a truncated series of spherical harmonics

$$x_S(\phi, \lambda) = \sum_{l,m}{}' a_{lm} Y_{lm}(\phi, \lambda), \qquad (6.1)$$

which has reduced contamination from Gibbs oscillations and does not substantially distort the true topographic features in $x(\phi, \lambda)$. The choice of coefficients a_{lm} is driven by a desire to obtain topography that is likely to produce more realistic climate simulations. Based on our evaluation of climate simulations using standard topography, the elimination of Gibbs ripples is expected to be a very important goal. Other objectives are the preservation of the height of major topographic barriers [since they are crucially linked to climate (Broccoli and Manabe 1992)] and the minimization of the broadening of the continents that occurs in truncated spherical harmonic representations of topography. Some methods for designing topography for spectral climate models are discussed in this section.

a. Nonuniform smoothing spline

A simple way of reducing the Gibbs oscillations is to represent topography by a smooth function. A method for generating smooth functions $x_S(\theta, \phi)$ approximating relatively rough surfaces $x(\theta, \phi)$ defined on the sphere, or fitting a smooth surface to a set of data on the sphere, is provided by the spherical smoothing spline described by Freedan (1981), Shure et al. (1982), Shure (1982), and Wahba (1981, 1982, 1990). The surface $x_S(\theta, \phi)$ defined by (6.1) is found by minimizing the constrained misfit

$$E = \int_{S_2} |x(\phi, \lambda) - x_S(\phi, \lambda)|^2 d\Omega + \Lambda \int_{S_2} |\nabla_S^2 x_S(\phi, \lambda)|^2 d\Omega \qquad (6.2)$$

with respect to a_{lm}, where the surface Laplacian

$$\nabla_S^2 = \frac{1}{\sin\phi}\frac{\partial}{\partial\phi}\left(\sin\phi\,\frac{\partial}{\partial\phi}\right) + \frac{1}{\sin^2\phi}\frac{\partial^2}{\partial\lambda^2},$$

so

$$\nabla_S^2 Y_{lm}(\phi, \lambda) = -l(l+1)Y_{lm}(\phi, \lambda).$$

The surface Laplacian constraint penalizes roughness in the model $x_S(\phi, \lambda)$ and in particular decreases oscillatory behavior such as Gibbs ripples. The Lagrange multiplier Λ describes the relative weighting given to the penalty [the second term in Eq. (6.2)] and the least squares misfit [the first term in Eq. (6.2)]. If $\Lambda = 0$, the topography minimizing E is the model given by (2.1) and (2.2). If $\Lambda \neq 0$,

$$a_{lm} = \frac{b_{lm}}{1 + \Lambda l^2(l+1)^2}. \qquad (6.3)$$

Shure (1982) describes a number of other constraints besides this squared-modulus surface Laplacian constraint. Unfortunately, these spherical smoothing spline methods do not provide a family of surfaces of sufficient richness to be useful for studying the interaction of global climate models with topography. In particular, spherical smoothing splines and related methods described by Shure (1982) of sufficient tautness to sig-

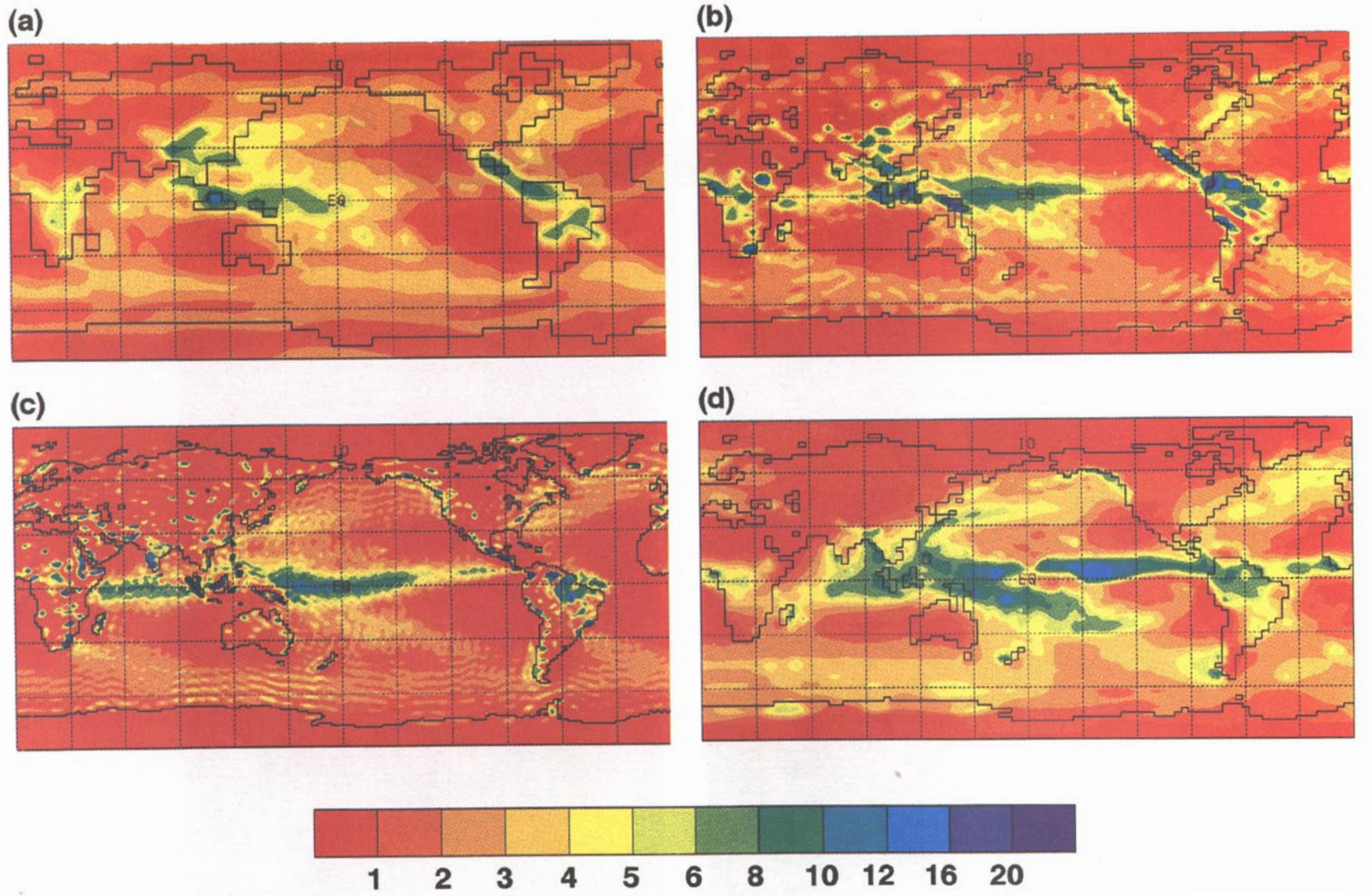

FIG. 4. Annual mean precipitation distributions (mm/day): (a) R15 simulation with standard topography; (b) R30 simulation with standard topography; (c) R63 simulation with standard topography; (d) observed data of Legates and Willmott (1990).

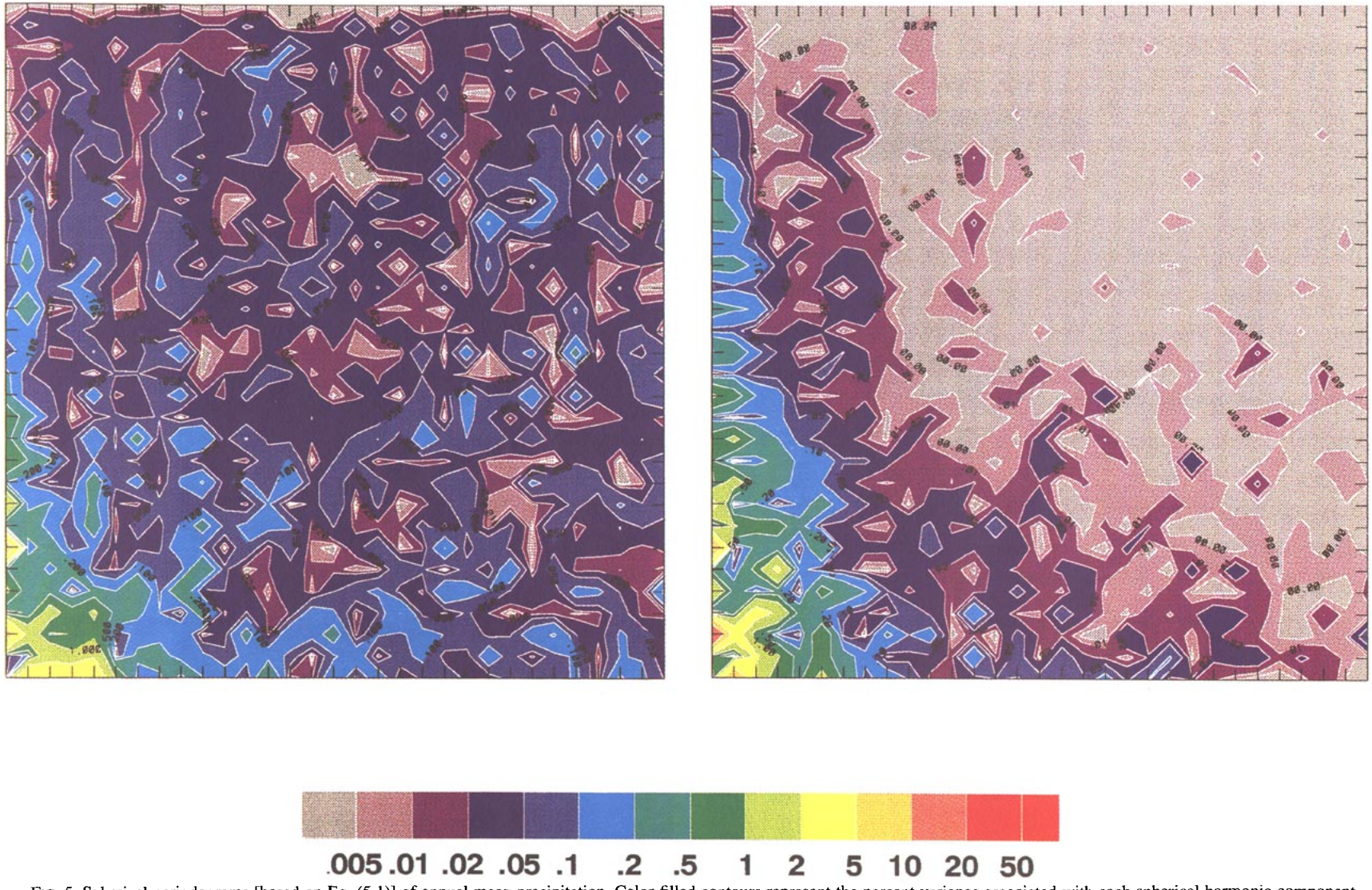

FIG. 5. Spherical periodograms [based on Eq. (5.1)] of annual mean precipitation. Color-filled contours represent the percent variance associated with each spherical harmonic component, with zonal wavenumber m on the abscissa and the shifted 8meridional wavenumber $l - |m|$ on the ordinate. Left: R30 simulation with standard topography. Right: Observed data of Legates and Willmott (1990).

nificantly reduce Gibbs oscillation amplitudes produce overly smooth topography with very little mountain relief and excessively broad continents.

A simple generalization of the spherical smoothing spline that we have found useful applies the surface Laplacian constraint over a restricted region Θ that does not contain topographic features of substantial relief; therefore, we minimize

$$\int_{S_2} |x(\phi, \lambda) - x_S(\phi, \lambda)|^2 d\Omega + \Lambda \int_{\Theta} |\nabla_S^2 x_S(\phi, \lambda)|^2 d\Omega \quad (6.4)$$

with respect to a_{lm}. While this constraint penalizes the Gibbs ripples only over the region Θ, if this region is of substantial size, the ripples will be reduced throughout the model $x_S(\phi, \lambda)$. A useful and easy choice of Θ is the region of the globe covered by oceans.

To minimize (6.4), an iterative scheme is adopted:

$$a_{lm}^{(j)} = a_{lm}^{(j-1)} + H_{lm}(b_{lm} - a_{lm}^{(j-1)}) + \Lambda H_{lm} \sum_{l'm'}{}' D_{lm}^{l'm'} a_{l'm'}^{(j-1)}, \quad (6.5)$$

where b_{lm} are the L_2 coefficients described by (2.2);

$$D_{lm}^{l'm'} = l(l+1)l'(l'+1) \int_{\Theta} Y_{l'm'}(\phi, \lambda) Y_{lm}^{*}(\phi, \lambda) d\Omega$$

and

$$H_{lm} = (1 + |\Lambda| D_{lm}^{lm})^{-1}$$

are the components of a preconditioning matrix that transforms the iteration (6.5) into a contraction mapping, making it a form of successive approximation (Luenberger 1969, section 10.2). Equations (2.2) or (6.3) can be used to produce starting values for the coefficients. Steepest descent (Curry 1944) or conjugate gradient algorithms (Daniel 1967) may result in more rapidly converging iterative schemes.

This regularization procedure produces surfaces $x_S(\phi, \lambda)$ that do not suffer from significantly decreased relief while essentially eliminating the Gibbs oscillations in meridional cross sections of the topography and reducing their amplitude in zonal cross sections of the topography. Since for some applications, the elimination of the zonal Gibbs ripples might be of equal or greater importance than the attenuation of the meridional ripples, this procedure may be inadequate. To simultaneously remove the Gibbs oscillations in both zonal and meridional directions while not distorting the relief, we investigated combining the regularization procedure with the use of special zonal filters, as described in the following section.

b. Combining the generalized smoothing spline with a zonal filter

Since the modulus-squared surface Laplacian constraint preferentially penalizes the meridional Gibbs oscillations relative to the zonal Gibbs oscillations, the regularization procedure in section 6a must be modified to produce topography on the sphere with reduced-amplitude Gibbs oscillations in both meridional and zonal directions without overly flattening the topographic relief. Two satisfactory methods have been found.

A zonal smoothing procedure can be used to produce a surface with minimal energy at the characteristic Gibbs frequency, $M + 1/2$. This can be done by convolving the original grid topography at each colatitude of ϕ with a boxcar of length $(M + 1/2)^{-1}$ [i.e., a moving average or Lanczos filter (Lanczos 1966; Hamming 1977)], or by applying a more sophisticated procedure such as a filter produced using concentration methods, as discussed in section 8. This zonally smoothed field can then be used in place of the true topography $x(\phi, \lambda)$ in (6.4). This results in surfaces that have reduced Gibbs oscillations while retaining more of the topographic relief than methods such as Cesàro summation (Lanczos 1966; Hamming 1977; Körner 1988) or two-dimensional Lanczos filtering.[3]

An alternative method that produces attractive topographic surfaces is similar to the method of projection on convex sets (POCS) (Biemond et al. 1990). Suppose that the action of a zonal filter, such as a Lanczos filter, in the spectral domain is denoted as an operator $S\{\ \}$. That is, if $x(\phi, \lambda)$ is some topographic model with spherical harmonic coefficients c_{lm} and $\tilde{x}(\phi, \lambda)$ is a zonally smoothed version of $x(\phi, \lambda)$ with spherical harmonic coefficients d_{lm}, then

$$d_{lm} = S\{c_{lm}\}. \quad (6.6)$$

This zonal smoothing is applied after each iteration (6.5):

[3] While the zonal Gibbs oscillations are well approximated by a single harmonic of frequency $M + 1/2$, the meridional Gibbs ripples in a rhomboidally truncated spherical harmonic series are better represented as a pair of sinusoids, closely spaced about frequency $M + 2.5$, in the middle of the spectrum of the rhomboidally truncated topography. A two-dimensional Lanczos filter can be constructed by convolving grid values of constant latitude with a boxcar of length $(M + 1/2)^{-1}$ and convolving grid values of constant longitude with a boxcar of length $(M + 2.5)^{-1}$. Unfortunately, features with substantial relief in meridional sections are smoothed out considerably by this procedure. This is because the high-frequency components that endow a feature with its steepness and some of its height are multiplied by the lower sidelobes of the sinc function when the Lanczos filter is applied, by the convolution theorem. This is less of a problem when smoothing zonal Gibbs oscillations because the zonal Gibbs frequency is at the edge of the topography spectrum rather than the middle.

$$a_{lm}^{(j)} = S\{a_{lm}^{(j-1)} + H_{lm}(b_{lm} - a_{lm}^{(j-1)}) + \Lambda H_{lm} \sum_{l'm'}{}' D_{lm}^{l'm'} a_{l'm'}^{(j-1)}\}. \quad (6.7)$$

This results in a topography with smaller zonal Gibbs oscillations compared to the iteration (6.5) without smoothing and, depending on the zonal smoother, may preserve much of the surface relief. We call a surface produced by the iterations (6.5) or (6.7) a "regularized topography." In this study, we produce regularized topography using the iteration (6.7) with a Lanczos filter as the zonal smoother, so

$$S\{c_{lm}\} = \frac{\sin(2\pi m/M)}{2\pi m/M}. \quad (6.8)$$

The resulting topography is evaluated in the following section.

c. *Regularized topography*

The regularized topography produced by combining the Lanczos filter and the regularization procedure, as described by (6.7), is compared to two other representations of topography formed by an R30 expansion in spherical harmonics: the standard topography generated as described in section 5 (and used in the climate model integrations described therein), and a version produced using the isotropic filter of Navarra et al. (1994) [a two-dimensional version of Cesàro summation, or Fejér smoothing (Lanczos 1966; Hamming 1977; Körner 1988)]. The Lagrange multiplier Λ appearing in (6.7) was chosen by trial to be -5×10^{-5} when fitting an R30 spherical harmonic expansion to the surface elevation.

The amplitude of the Gibbs oscillations varies considerably among the different representations of spectral topography. The regularized topography has the smallest Gibbs oscillations (Fig. 6a). They are somewhat larger in the isotropic version (Fig. 6b), particularly the zonal Gibbs oscillations, and much larger in the standard topography (Fig. 2). Figure 7, a cross section along 21°S, illustrates this dramatically by comparing the ripples extending westward across the Pacific from the Andes for each surface. The remaining "valleys" over oceanic regions tend to be broader and shallower in the regularized topography, and are most notable in the Arctic Ocean and just off the coasts of Greenland, Antarctica, and the Americas.

There is also considerable variation in the height of topographic barriers among the different representations. The peaks of both the isotropic and regularized topography are lower than the corresponding local maxima of the original gridpoint surface and the standard topography. (Note that the standard version also unrealistically overshoots the height of the original topography in some places.) In the case of very sharp, narrow mountain barriers such as the Andes, the isotropic topography retains more of the peak elevation than the regularized version, as is evident from Fig. 7. However, for broader features such as Greenland, southern Africa, and the Tibetan and East Antarctic Plateaus, the regularization method preserves more of the original terrain height than the isotropic procedure. This is illustrated in the cross sections along 86°E (Fig. 8).

In both the isotropic and regularized versions, a broadening of the continents is among the costs associated with the reduction of the Gibbs oscillations. The broadening is more pronounced in the regularized version, and is apparent in both the maps and the cross sections. There are other techniques available for representing spectral topography that may be able to reduce the amount of broadening associated with a given reduction of the Gibbs ripples, but these were not attempted in this study. They are discussed briefly in section 8.

A penalty function that treats the misfit of the model differently in continental and oceanic regions was also used in the recent work of Bouteloup (1995). Bouteloup suggests using a fourth power cost function for the misfit of the model in oceanic areas and a second power cost function for the misfit over land (or a similar but more complicated penalty function depending on several free parameters).

However, the regularization method described here differs from the work of Bouteloup (1995). Not only does (6.7) depend on only one free parameter, the Lagrange multiplier Λ, but it penalizes oscillatory behavior in the spectral topography, while Bouteloup's penalty function simply imposes a greater cost on oceanic misfit than on continental misfit. Also, the regularization method reduces Gibbs oscillations globally, while Bouteloup's method results in a surface with numerous Gibbs truncation artifacts in the Southern Hemisphere, while reducing them in areas close to Europe (which may be sufficient for regional numerical weather prediction).

To summarize, the regularization technique seems to be quite successful at reducing the magnitude of the Gibbs oscillations in both the zonal and meridional directions without an unacceptable reduction of the height of mountain barriers. The topography that results is quite faithful to the large-scale patterns of surface relief, although the continents are broader and some narrow mountain ranges are reduced in height. In the following section we describe a climate model integration performed with the regularized topography and compare the simulated precipitation with that from integrations using other representations of topography.

7. Regularized topography and simulated precipitation

The regularized topography was used as a lower boundary surface for an integration of the climate model at R30 resolution. To place the results from this

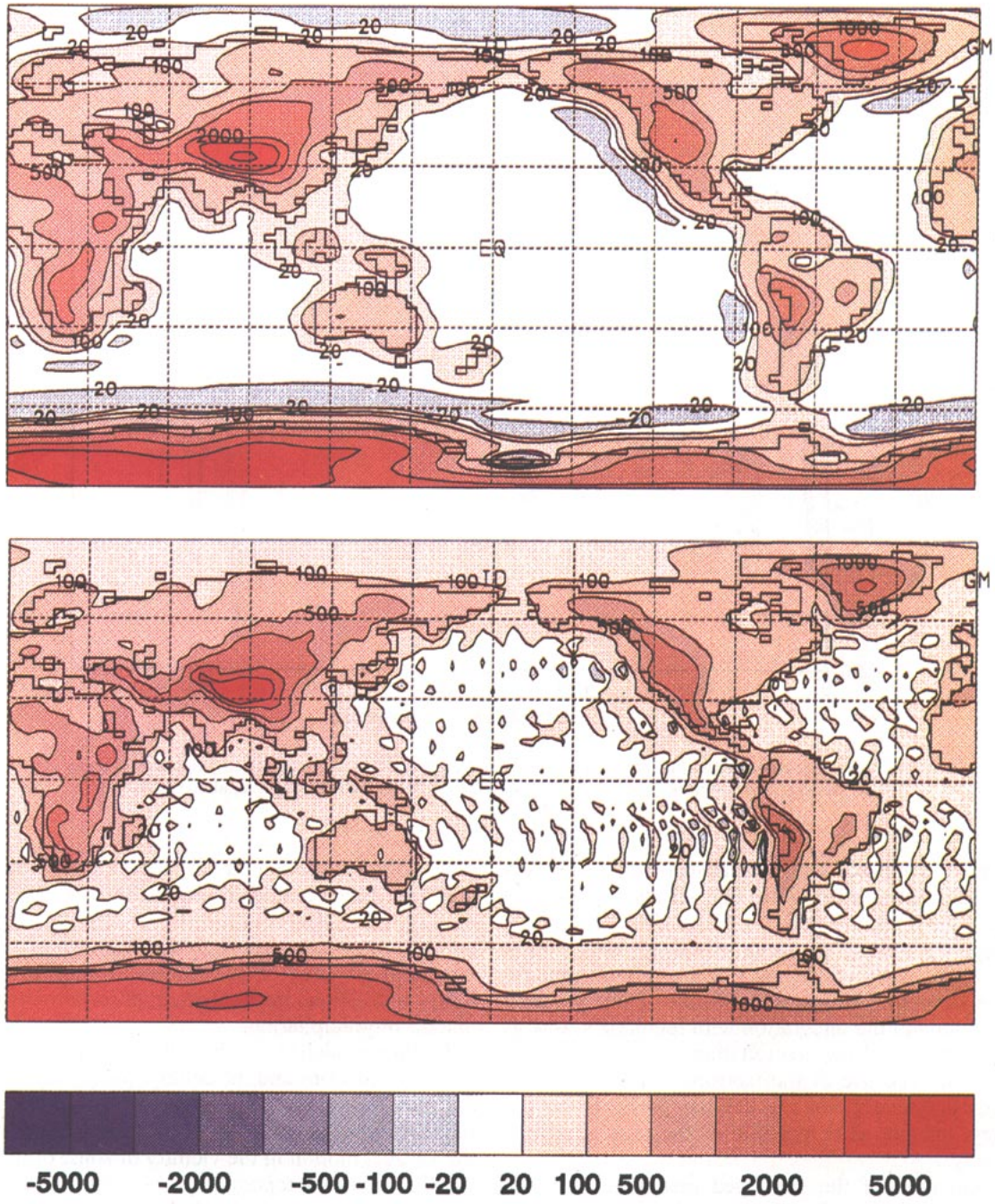

FIG. 6. Surface elevation (m). Top: R30 regularized topography. Bottom: R30 isotropic-filtered topography.

integration into context, an additional run was made using the isotropic topography of Navarra et al. (1994), since it represents one of the best techniques for globally reducing the Gibbs oscillations among those in the literature. All other aspects of these integrations were identical to the one conducted using the standard topography, as described in section 5.

A comparison of the precipitation from the integrations with the standard, isotropic, and regularized topography to the observed climatology of Legates and Willmott (1990) provides an indication of its sensitivity to the representation of topography. Maps of the annual mean precipitation for the isotropic and regularized topography integrations are presented in Fig. 9,

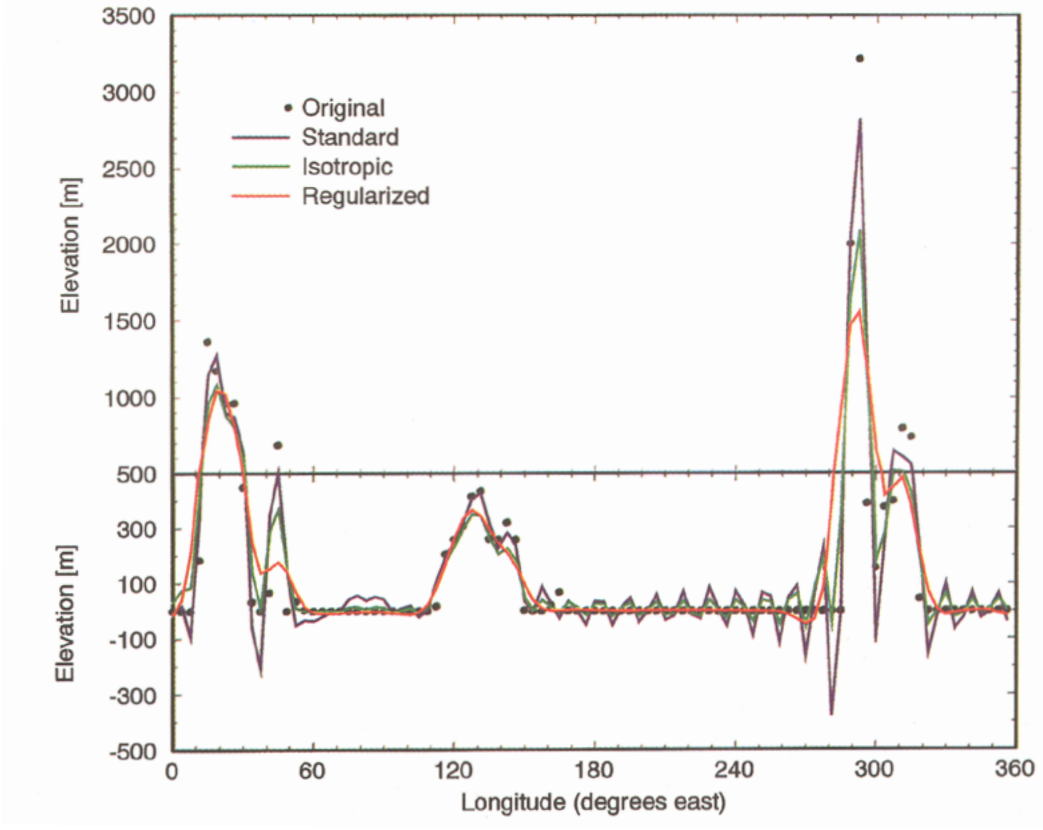

FIG. 7. Surface elevation profiles (m) along 21°S from four different R30 topographies: original grid point (black circles), standard truncation (blue line), isotropic filtered (green line), and regularized (red line).

and can be compared with similar maps from the standard topography integration (Fig. 4) and the data of Legates and Willmott (Fig. 4). Substantial differences are apparent among the three simulated precipitation fields, particularly with regard to the cellular precipitation pathology. Almost no evidence of this problem can be found in the integration with regularized topography, as the resulting precipitation is rather smoothly distributed. The use of the isotropic topography also reduces the severity of the cellular precipitation pathology, but not as completely as the regularized topography.

Examination of the simulated precipitation in the spectral domain confirms the results obtained from comparing the distributions of precipitation in physical space. Spherical periodograms of annual precipitation from the isotropic and regularized topography integrations (Fig. 10) can be compared with those from the standard topography integration and the observed climatology (Fig. 5). The substantial decrease in the fractional variance associated with high zonal and meridional wavenumbers for the isotropic and regularized topography integrations results from reductions in the cellular precipitation pathology. The spectral distribution of precipitation from the regularized topography integration is very similar to the spectral distribution of observed precipitation, especially at high wavenumbers. While differences are still evident at low wavenumbers, this suggests that the removal of spurious variations on small spatial scales associated with the Gibbs oscillations may be essential for a realistic simulation of precipitation.

Further evidence of the relationship between the Gibbs oscillations and the cellular precipitation pathology can be obtained by a closer examination of the model output. In particular, it is enlightening to study the vertical motion in the vicinity of some of the Gibbs oscillations in the topography. As a way of identifying the Gibbs oscillations, we decompose the standard topography into the sum of two components: a smooth portion and a part containing the Gibbs oscillations. Representing the smooth piece by the regularized topography, the Gibbs component can be estimated as the difference between the standard topography and the regularized topography. This quantity is depicted for southern Asia and the surrounding area in the top half of Fig. 11. A "checkerboard" pattern of alternating maxima and minima (with magnitudes often greater than 500 m) is evident in the vicinity of the Tibetan Plateau. In comparing this pattern to the annual mean

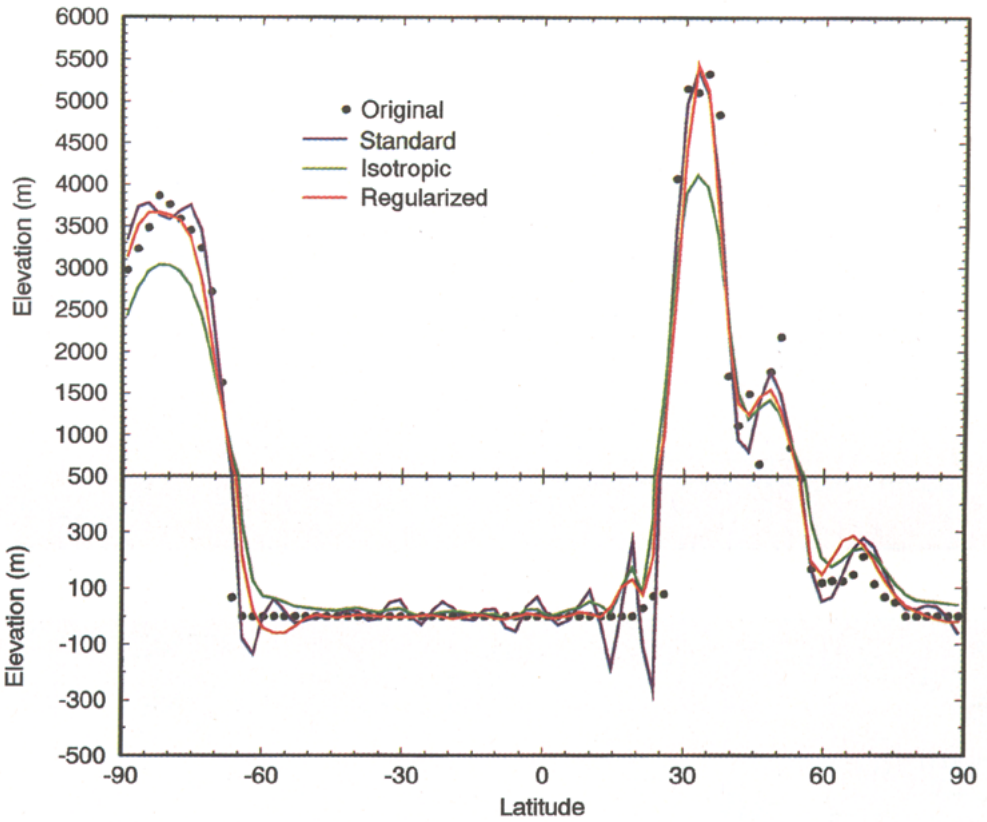

FIG. 8. Same as Fig. 7 except along 86°E.

vertical pressure velocity in the midtroposphere from the integration with standard topography (Fig. 11, bottom), a strong relationship is evident, with sinking motion coincident with the Gibbs oscillation "valleys" and rising motion above the Gibbs "peaks." The spatial distribution of vertical motion is thus dominated by a noisy, small-scale pattern, which is probably the result of the Gibbs oscillations. Many of the precipitation maxima responsible for the cellular precipitation pathology (see Fig. 4b) are associated with areas of rising motion resulting from the Gibbs ripples.

It is useful to try to quantify these changes in simulated precipitation that occur in response to changes in the representation of topography. As in section 5, pattern correlation statistics and rms differences are used to describe the agreement between the observed data of Legates and Willmott (1990) and the annual mean precipitation in standard, isotropic, and regularized topography integrations. The results are listed in Tables 1 and 2. Isotropic and regularized topography integrations have substantially higher pattern correlations and lower rms differences than the standard topography integration. The overall pattern correlation of 0.737 for the regularized topography integration is the best among the R30 integrations and exceeds the best pattern correlation (0.717) from any integration employing standard topography (in this case, the R15). The regularized topography integration also has the lowest overall rms error (0.179 cm/day). Over the continents the improvement in the rms difference is particularly evident.

These statistics demonstrate that substantial improvement in the fidelity of simulated precipitation can be achieved by decreasing the amplitude of Gibbs oscillations in the model topography. Reducing Gibbs artifacts may also be a necessary condition to insure that precipitation simulations become more realistic with increasing horizontal resolution, since the results from the integrations with standard topography suggest that the deleterious effects of the Gibbs oscillations become more severe as resolution is increased.

8. Suggestions for further work

Further improvements in the representation of topography may be possible through the use of a more sophisticated technique relying on the study of concentration problems on the sphere. Versions of the topography designed this way are optimal in an information–theoretic sense and should result in more faithful representation of narrow mountain ranges and continental boundaries.

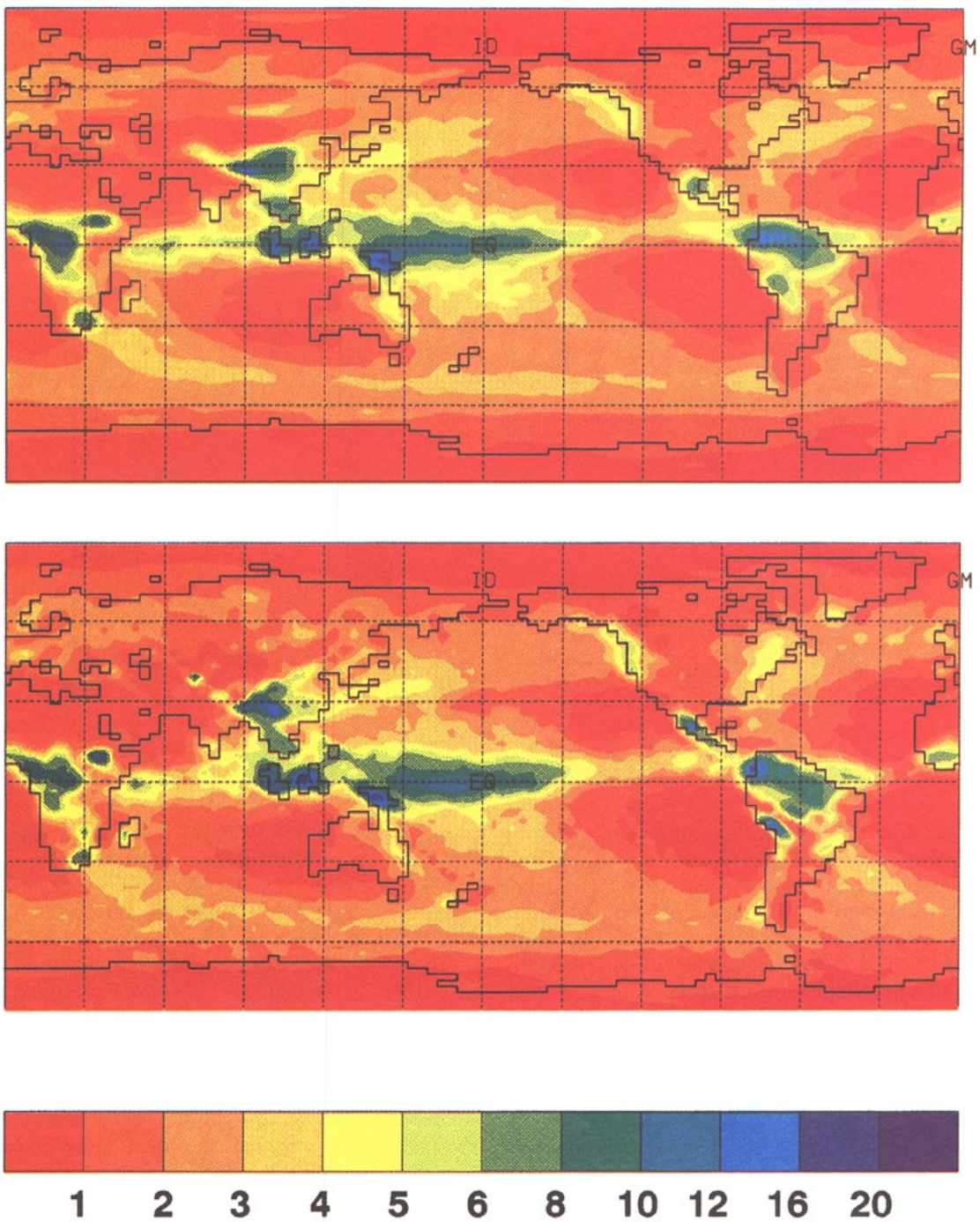

FIG. 9. Annual mean precipitation distributions (mm/day). Top: R30 simulation with regularized topography. Bottom: R30 simulation with isotropic-filtered topography.

The best understood concentration problem is one-dimensional; one seeks those band-limited functions whose Fourier transforms are most concentrated in a given interval in space. The solution to this problem is a family of useful functions called the prolate spheroidal wavefunctions; some of their properties are described in Slepian (1983). An expansion of the topography in terms of these special functions can be used to produce filtered topography that suffers very little from broadening of topographic features, such as coastlines and mountain ranges, while accurately representing orographic

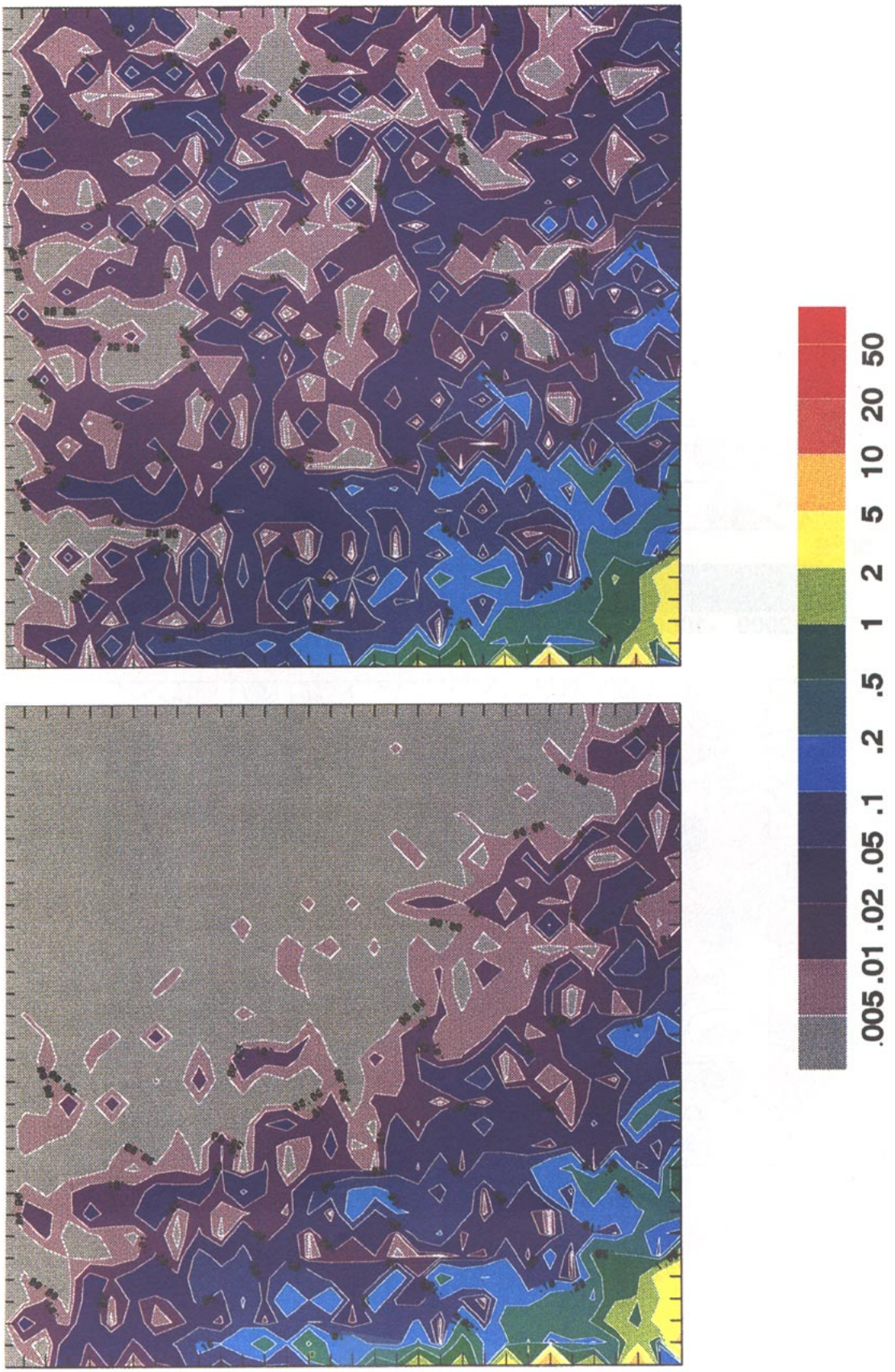

FIG. 10. Same as Fig. 5. Left: R30 simulation with regularized topography. Right: R30 simulation with isotropic-filtered topography.

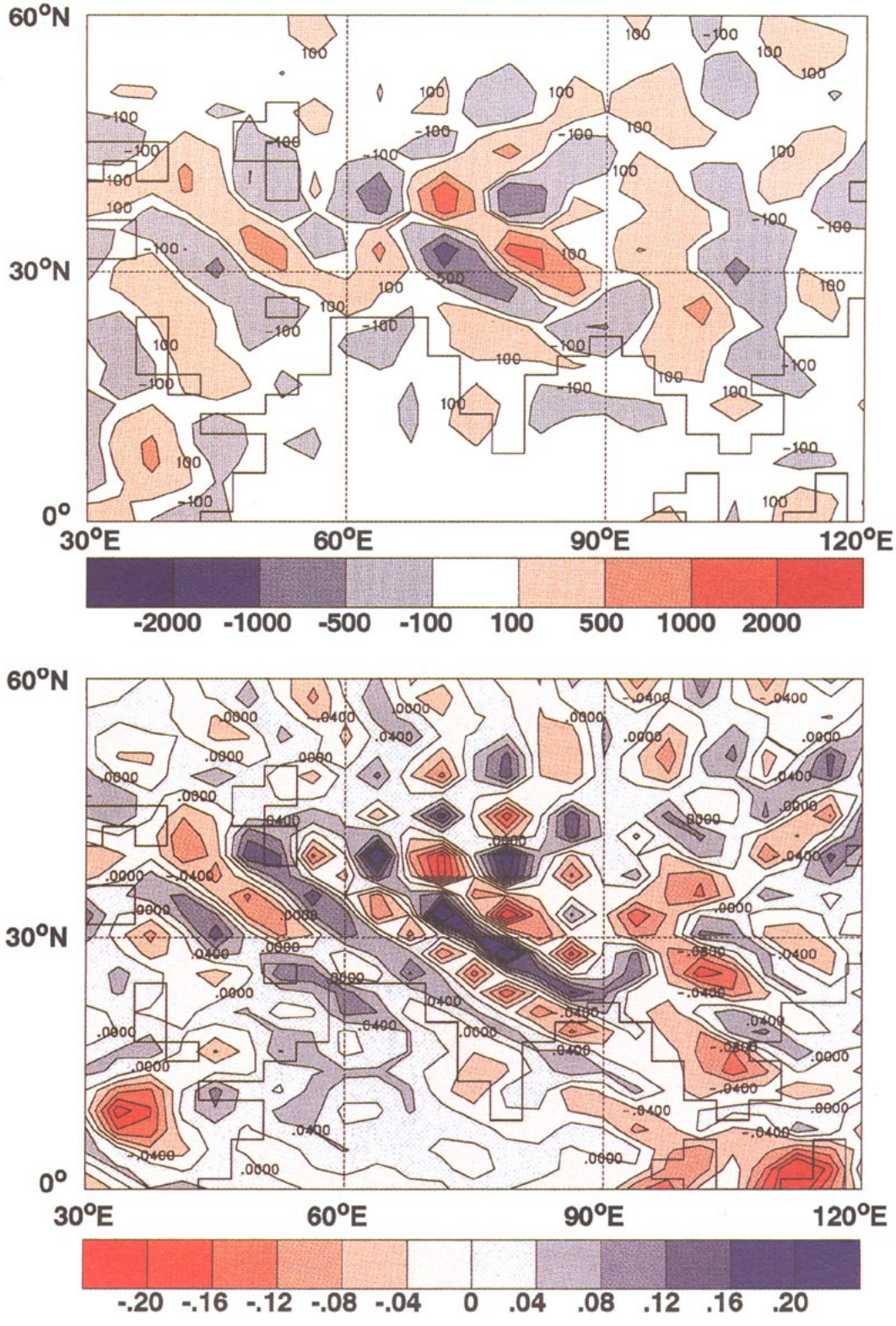

FIG. 11. Top: Difference in surface elevation (m) between the R30 standard and R30 regularized topographies for the Tibetan Plateau region. (This quantity is assumed to represent the Gibbs component of the R30 standard topography). Bottom: Annual mean vertical pressure velocity (Pa s^{-1}) at the $\sigma = 0.515$ level, where σ is the normalized pressure coordinate, from the R30 simulation with standard topography.

TABLE 1. Pattern correlations of simulated annual-mean precipitation with Legates and Willmott (1990) climatology. The correlations are computed globally for land points and for sea points.

	Pattern correlation		
Integration	Global	Land	Sea
R15 standard	0.717	0.764	0.724
R30 standard	0.660	0.720	0.712
R63 standard	0.549	0.506	0.671
R30 isotropic	0.722	0.811	0.728
R30 regularized	0.737	0.811	0.742

peak heights. Using these prolate wavefunction filters as zonal filters, as described in section 6b, reduces broadening distortions.

A more sophisticated approach to designing spectral model topography may be provided by extending the concentration problem methods from the circle to the sphere. This procedure would eliminate the need for complicated iterative searches or heuristic spectral coefficient weighting schemes. The work of Grunbaum et al. (1982) suggests a method for efficiently solving concentration problems on the sphere, in which the functions band limited to some region of $l - m$ space and most concentrated in some region on the sphere are sought. Presumably these functions could be employed in an expansion scheme for topography on the sphere similar to that described above to avoid excessive broadening of topographic features. Further work is necessary to determine if using these concentration problem techniques can be successfully adapted to the representation of topography in spectral models.

9. Conclusions

This study has demonstrated that the conventional representation of spectral model topography as a truncated set of spherical harmonics computed from grid-point data can produce highly undesirable effects on simulated precipitation in climate simulations. These effects are manifest as an accumulation of spatial variance in precipitation on very small scales, or what we have called the "cellular precipitation pathology." At the root of this pathology are ripples in the model topography, analogous to Gibbs oscillations in a truncated Fourier series, as described by Navarra et al. (1994). The resulting distortion of the precipitation field increases with horizontal resolution, making it a serious obstacle to the realistic simulation of hydrologic quantities on smaller scales.

We propose an alternative representation of spectral topography and demonstrate its use in a climate simulation. This representation utilizes a Lanczos filter as a zonal smoother in combination with a nonuniform version of the spherical smoothing spline. The topography that results from this iterative regularization procedure is largely free of the small-scale oscillations that characterize the standard topography. Furthermore, the precipitation from the climate simulation performed using this regularized topography is in substantially better agreement with the observed climatology, both in physical space and spectral space. It also improves on the simulated precipitation produced using previously available techniques for reducing Gibbs oscillations (Navarra et al. 1994). In fact, the reduction of Gibbs oscillations in spectral topography seems to be an essential requirement for improved simulation of hydrologic quantities as the horizontal resolution of climate models increases.

An examination of climate simulations produced for the Atmospheric Model Intercomparison Project (Gates 1992) reveals that Gibbs oscillations are present in the topography used by many other spectral climate modeling groups. This suggests that the phenomenon described in this paper may have broad impact, although it is possible that the particular combination of physical parameterizations used in the GFDL climate model makes it more sensitive to this problem. Some evidence of Gibbs artifacts are present in maps of cloud statistics from the ECMWF model (Potter et al. 1992), suggesting that precipitation could be similarly affected.

The sensitivity of the spatial pattern of precipitation to the model topography raises a question about the realism of the precipitation fields simulated using the regularized topography. Since much of the world's precipitation is produced by weather systems with rather small scales, how reasonable are the smooth precipitation fields produced from observations (Figs. 4d and 5) or simulated using the regularized topography (Figs. 9 and 10)? An important consideration in answering this question is the timescale of interest. Over flat terrain, inhomogeneities in the spatial distribution of precipitation can be very large over short time periods (i.e., days), but these become smaller as the length of the averaging period is increased (D. R. Legates 1994, personal communication; C. J. Willmott 1994, personal communication). In areas of significant relief, the geographic distribution of precipitation producing systems

TABLE 2. Root-mean-square differences (cm/day) between simulated annual mean precipitation and Legates and Willmott (1990) climatology. The root-mean-square differences are computed globally for land points and for sea points.

	Rms difference		
Integration	Global	Land	Sea
R15 standard	0.180	0.175	0.182
R30 standard	0.209	0.242	0.192
R63 standard	0.263	0.352	0.212
R30 isotropic	0.185	0.183	0.186
R30 regularized	0.179	0.175	0.181

is often strongly influenced by the topographic features, so that spatial inhomogeneities persist even as longer averaging periods are used. This is evident when examining long-term averages of observed precipitation from regions where the density of observations is high, such as the central and eastern United States (e.g., U.S. Environmental Data Service 1968). For multiyear averages of simulated precipitation such as those examined in this study, orographically induced extrema are realistic only if the topographic features that produce them are realistic features of the earth's topography that can be resolved at the horizontal resolution of the model. At the R30 resolution used in most of these experiments, only relatively large-scale topographic features (e.g., the Tibetan Plateau, Antarctic ice sheet, Rocky/Andes cordillera) can be resolved without introducing Gibbs artifacts, so it is reasonable for precipitation extremes associated with smaller features (e.g., the Alps, Atlas Mountains, Tien Shan) to be absent from the simulated precipitation fields. We therefore argue that multiyear averages of annual observed and simulated precipitation should be relatively smooth, although precipitation maxima and minima associated with resolvable orographic features should be evident.

While the regularization method described here reduces the magnitude of the cellular precipitation pathology and is better at eliminating small-scale ripples and maintaining the height of broad topographic features than techniques previously proposed for reducing Gibbs oscillations, its drawbacks include a substantial broadening of the continents and a serious reduction in the height of very narrow mountain ranges. The broadening of continents and narrow topographic features, such as the Andes, is partly a consequence of the zonal filtering described in section 6b. It is possible that this broadening may cause difficulties for the simulation of aspects of climate not considered in our analysis. For example, continental broadening may produce inaccurate simulations of oceanic fields in coupled models. However, designing filters based on the solution of concentration problems originating in communication theory may alleviate some of the difficulties with representing narrow topographic features using only a few spectral coefficients.

It should also be noted that the version of the regularization procedure used here was designed specifically to produce R30 topography with the desired attributes. Slightly modified procedures may be necessary to generate topographies with the same attributes when different truncations (such as R15, R63, and T42, for example) are used. Careful experimentation may be required to arrive at the modifications that achieve the desired reduction of Gibbs ripples, but such effort may be well spent in avoiding their destructive effects on the simulation of hydrologic quantities.

Acknowledgments. We thank S. Manabe for his support of this work, J. Anderson, Y. Hayashi, and the anonymous reviewers for their comments, and C. Raphael and J. Varanyak for their help in preparing the illustrations.

REFERENCES

Biemond, J., R. L. Lagendijk, and R. M. Mersereau, 1990: Iterative methods for image deblurring. *Proc. IEEE,* **78,** 856–883.

Bourke, W., 1974: A multi-level model. 1. Formulation and hemispheric integrations. *Mon. Wea. Rev.,* **102,** 687–701.

Bouteloup, Y., 1995: Improvement of the spectral representation of the earth topography with a variational method. *Mon. Wea. Rev.,* **123,** 1560–1573.

Boville, B. R., 1991: Sensitivity of simulated climate to model resolution. *J. Climate,* **4,** 469–485.

Broccoli, A. J., and S. Manabe, 1992: The effects of orography on midlatitude Northern Hemisphere dry climates. *J. Climate,* **5,** 1181–1201.

Canuto, C., M. Y. Hussaini, A. Quarteroni, and T. A. Zang, 1988: *Spectral Methods in Fluid Dynamics.* Springer-Verlag, 557 pp.

Cuming, M. J., and B. A. Hawkins, 1981: TERDAT: The FNOC system for terrain data extraction and processing. FNOC Tech. Rep. [Available from Fleet Numerical Oceanography Center, 7 Grace Hopper Avenue, Monterey, CA 93943.]

Curry, H. B., 1944: The method of steepest descent for nonlinear optimization problems. *Quart. Appl. Math.,* **2,** 258–261.

Daniel, J. W., 1967: The conjugate gradient method for linear and nonlinear operator equations. *SIAM J. Numer. Anal.,* **4,** 10–25.

Freeden, W., 1981: On spherical spline interpolation and approximation. *Math. Methods Appl. Sci.,* **3,** 551–575.

Gates, W. L., 1992: AMIP: The Atmospheric Model Intercomparison Project. *Bull. Amer. Meteor. Soc.,* **73,** 1962–1970.

Gordon, C. T., and W. F. Stern, 1982: A description of the GFDL global spectral model. *Mon. Wea. Rev.,* **110,** 625–644.

Grunbaum, F. A., L. Longhi, and M. Perlstadt, 1982: Differential operators commuting with finite convolution integral operators: Some non-Abelian examples. *SIAM J. Appl. Math,* **42,** 941–955.

Hamming, R. W., 1977: *Digital Filters.* Prentice-Hall, 226 pp.

Hobson, E. W., 1931: *The Theory of Spherical and Ellipsoidal Harmonics.* Cambridge University Press, 500 pp.

Hoskins, B. J., 1980: Representation of the earth topography using spherical harmonics. *Mon. Wea. Rev.,* **108,** 111–115.

Hulme, M., 1991: An intercomparison of model and observed global precipitation climatologies. *Geophys. Res. Lett.,* **18,** 1715–1718.

Jones, M. N., 1985: *Spherical Harmonics and Tensors for Classical Field Theory.* John Wiley and Sons, 230 pp.

Körner, T. W., 1988: *Fourier Analysis.* Cambridge University Press, 591 pp.

Lacis, A. A., and J. E. Hansen, 1974: A parameterization for the absorption of solar radiation in the earth's atmosphere. *J. Atmos. Sci.,* **31,** 118–133.

Lanczos, C., 1966: *Discourse on Fourier Series.* Oliver & Boyd, 255 pp.

Legates, D. R., and C. J. Willmott, 1990: Mean seasonal and spatial variability in gauge-corrected global precipitation. *Int. J. Climatol.,* **10,** 111–127.

Luenberger, D. G., 1969: *Optimization by Vector Space Methods.* John Wiley and Sons, 326 pp.

Manabe, S., 1969: Climate and the ocean circulation. I. The atmospheric circulation and the hydrology of the earth's surface. *Mon. Wea. Rev.,* **97,** 739–774.

Navarra, A., W. F. Stern, and K. Miyakoda, 1994: Reduction of the Gibbs oscillation in spectral model simulations. *J. Climate,* **7,** 1169–1183.

Potter, G. L., J. M. Slingo, J.-J. Morcrette, and L. Corsetti, 1993: A modeling perspective on cloud radiative forcing. *J. Geophys. Res.,* **97,** 20 507–20 518.

Shure, L., 1982: Modern mathematical methods in geomagnetism. Ph.D. thesis, University of California, San Diego, 140 pp.

——, R. Parker, and G. Backus, 1982: Harmonic splines for geomagnetic modelling. *Phys. Earth Planet. Inter.*, **28,** 215–229.

Slepian, D., 1983: Some comments on Fourier analysis, uncertainty and modeling. *SIAM Rev.*, **25,** 379–393.

Stone, H. M., and S. Manabe, 1968: Comparison among various numerical models designed for computing infrared cooling. *Mon. Wea. Rev.*, **96,** 735–741.

U.S. Environmental Data Service, 1968: *Climatic Atlas of the United States,* Superintendent of Documents, Washington, DC, 80 pp.

Wahba, G., 1981: Spline interpolation and smoothing on the sphere. *SIAM J. Sci. Statist. Comput.*, **2,** 5–16.

——, 1982: Erratum: Spline interpolation and smoothing on the sphere. *SIAM J. Sci. Statist. Comput.*, **3,** 385–386.

——, 1990: *Spline Models for Observational Data.* CBMS–NSF Regional Conference Series in Applied Mathematics, Society of Industrial and Applied Mathematics, 169 pp.